11438 *Biochemistry* **1994,** *33,* 11438–11452

Sequential ^{1}H, ^{13}C, and ^{15}N NMR Assignments and Solution Conformation of Apokedarcidin[†]

Keith L. Constantine,[*,‡] Kimberly L. Colson,[§,∥] Michael Wittekind,[‡] Mark S. Friedrichs,[‡] Nada Zein,[‡]
Jeffrey Tuttle,[‡] David R. Langley,[§] John E. Leet,[§] Daniel R. Schroeder,[§] Kin S. Lam,[§] Bennett T. Farmer II,[‡]
William J. Metzler,[‡] Robert E. Bruccoleri,[‡] and Luciano Mueller[‡]

Bristol-Myers Squibb Pharmaceutical Research Institute, Princeton, New Jersey 08543-4000, and Bristol-Myers Squibb Pharmaceutical Research Institute, Wallingford, Connecticut 06492

Received April 27, 1994; Revised Manuscript Received June 30, 1994[⊗]

ABSTRACT: Kedarcidin is a recently discovered antitumor antibiotic chromoprotein. The solution conformation of the kedarcidin apoprotein (114 residues) has been characterized by heteronuclear multidimensional NMR spectroscopy. Sequence-specific backbone atom resonance assignments were obtained for a uniformly ^{13}C/^{15}N-enriched sample of apokedarcidin *via* a semiautomated analysis of 3D HNCACB, 3D CBCA(CO)NH, 4D HNCAHA, 4D HN(CO)CAHA, 3D HBHA(CO)NH, and 3D HNHA(Gly) spectra. Side-chain assignments were subsequently obtained by analysis of (primarily) 3D HCCH-TOCSY and HCCH-COSY spectra. A qualitative analysis of the secondary structure is presented on the basis of $^3J_{\alpha\mathrm{NH}}$ coupling constants, deviations of ^{13}C$^\alpha$ and ^{13}C$^\beta$ chemical shifts from random coil values, and NOEs observed in 3D ^{15}N- and ^{13}C-edited NOESY-HSQC spectra. This analysis revealed a four-stranded antiparallel β-sheet, a three-stranded antiparallel β-sheet, and two two-standed antiparallel β-sheets. The assignments of cross-peaks in the 3D NOESY spectra were assisted by reference to a preliminary model of apokedarcidin built using the program CONGEN starting from the X-ray structure of the homologous protein aponeocarzinostatin. An ensemble of 15 apokedarcidin solution structures has been generated by variable target function minimization (DIANA program) and refined by simulated annealing (X-PLOR program). The average backbone atom root-mean-square difference between the individual structures and the mean coordinates is 0.68 ± 0.08 Å. The overall fold of apokedarcidin is well-defined; it is composed of an immunoglobulin-like seven-stranded antiparallel β-barrel and a subdomain containing two antiparallel β-ribbons. Highly similar tertiary structures have been previously reported for the related proteins neocarzinostatin, macromomycin, and actinoxanthin. Important structural features are revealed, including the dimensions of the chromophore-binding pocket and the locations of side chains that are likely to be involved in chromophore stabilization.

Kedarcidin is a recently isolated chromoprotein (M_r ~12.4K) consisting of a labile nine-membered ring enediyne that is noncovalently associated with an acidic, stabilizing polypeptide of 114 amino acid residues (Lam et al., 1991; Hofstead et al., 1992; Leet et al., 1992). Derived from the culture supernatant of actinomycete strain L585-6 (ATCC 53650), kedarcidin displays potent antitumor activity, as well as antimicrobial activity against Gram-positive bacteria (Lam et al., 1991). The chromophore (Leet et al., 1993), which has been shown to cleave DNA[1] in a sequence-specific manner (Zein et al., 1993a), is a member of the enediyne class of cytotoxic antitumor antibiotics (Nicolaou & Dai, 1991). Other compounds in this class include the 10-membered ring enediynes—esperamicin, calicheamicin, and dynemicin—for which no associated proteins have been found (Golik et al., 1987a,b; Konishi et al., 1989; Lee et al., 1992) and neocarzinostatin, which, like kedarcidin, consists of an acidic protein complexed with a labile nine-membered ring enediyne (Edo et al., 1985; Hensens et al., 1989; Hensens & Goldberg, 1989; Goldberg, 1991).

The antitumor and antimicrobial activities of the enediynes are primarily due to their DNA-cleaving abilities (Nicolaou & Dai, 1991). In the cases of kedarcidin and neocarzinostatin, the protein is believed to stabilize the associated chromophore and deliver it to the appropriate site before dissociation (Zein et al., 1993b, and references therein). Additionally, it has recently been demonstrated that kedarcidin possesses specific proteolytic activity, particularly against highly basic histone proteins (Zein et al., 1993b). These data, along with observations that the apoprotein enhances the activity of the chromophore (Zein et al., 1993b), suggest that kedarcidin mounts a "two-pronged" attack, with the protein functioning both to stabilize the chromophore and to cleave histones. This latter activity may serve to disrupt the chromatin superstructure and expose additional DNA to the highly reactive chromophore.

In addition to kedarcidin and neocarzinostatin, other related chromoproteins exhibiting DNA-damaging activity include auromomycin (Yamashita et al., 1979; Kumada et al., 1983), which is also known macromomycin (Chimura et al., 1968;

[†] The coordinates of the 15 NMR structures have been deposited with the Protein Data Bank, Brookhaven National Laboratory, Upton, NY 11973. The access number is 1AKP.

[*] To whom correspondence should be addressed.

[‡] Bristol-Myers Squibb Pharmaceutical Research Institute, P.O. Box 4000, Princeton, NJ 08543.

[§] Bristol-Myers Squibb Pharmaceutical Research Institute, Wallingford, CT 06492.

[∥] Current address: Burroughs Wellcome, Research Triangle Park, NC 27709.

[⊗] Abstract published in *Advance ACS Abstracts,* September 1, 1994.

[1] Abbreviations: ABNR, adopted-basis Newton–Raphson; CLPD, complex linear prediction; CW, continuous wave; DNA, deoxyribonucleic acid; FID, free induction decay; ge, gradient enhanced; HSQC, heteronuclear single-quantum coherence; NMR, nuclear magnetic resonance; NOE, nuclear Overhauser effect; NOESY, nuclear Overhauser effect spectroscopy; ppm, parts per million; REDAC, redundant dihedral angle constraint; rf, radio frequency; RMSD, root-mean-square difference; sw, spectral width; τ_m, mixing time; TOCSY, total correlation spectroscopy; 2D, two dimensional; 3D, three dimensional; 4D, four dimensional.

0006-2960/94/0433-11438$04.50/0

1 20 40

MCR -APGVT**V**T**P**AT**GL**SN**G**QT**V**T**V**SATGLTPG**T**VYHVG**QCA**VVEP**G**VI

AXN -APAFS**V**S**P**AS**GL**SD**G**QS**V**S**V**SGAAA-GE**T**-YYIA**QCA**PVG-**G**QD

NCS AAPTAT**V**T**P**SS**GL**SD**G**TV**V**K**V**AGAGLQAG**T**AYDVG**QCA**WVNT**G**VL

KED ASAAVS**V**S**P**AT**GL**AD**G**AT**V**T**V**SASGFATS**T**SATAL**QCA**ILAD**G**RG

60 80

MCR G**C**DATTSTDVTADAA**G**KITAQLK**V**HS**S**FQAVVGAD**G**TPW**G**T**V**N**C**K

AXN A**C**NPATATSFTTDAS**G**AASFSFT**V**RK**S**YAGQTP-S**G**TPV**G**S**V**D**C**A

NCS A**C**DPANFSSVTADAN**G**SASTSLT**V**RR**S**FEGFLF-D**G**TRW**G**T**V**D**C**T

KED A**C**NVAEFHDFSLS-G**G**EGTTSVV**V**RR**S**FTGYVMPD**G**PEV**G**A**V**D**C**D

100 114

MCR VVS--**C**SAGLGSDSGEGAA-Q**A**IT**F**A

AXN TDA--**C**NLGAGNSGLNLG-HV**A**LT**F**G

NCS TAA--**C**QVGLSDAAGNGPEGV**A**IS**F**N

KED TAPGG**C**EIVVGGNTGEYG-NA**A**IS**F**G

FIGURE 1: Amino acid sequence comparison of macromomycin (MCR; Samy et al., 1983), actinoxanthin (AXN; Gibson et al., 1984), neocarzinostatin (NCS; Adjadj et al., 1990), and kedarcidin (KED; Hofstead et al., 1992). Residues which are absolutely conserved in all four proteins are shown in bold type, and the kedarcidin sequential numbering is shown above the sequences.

Hidaka et al., 1979; Zaheer et al., 1985; Vay Roey & Beerman, 1989) in its predominantly apo form, C-1027 (Sakata et al., 1992; Otani, 1993), and actinoxanthin (Khokhlov et al., 1969, 1976). The protein component of a sixth antitumor chromoprotein, maduropeptin (M_r ~22.5K), is not related to the kedarcidin class of proteins (Hanada et al., 1991; Hans Marquardt, personal communication). The conformations of macromomycin, actinoxanthin, and neocarzinostatin have been investigated by X-ray crystallography. A medium (2.5-Å) resolution X-ray crystallographic structure of apoactinoxanthin has been reported (Pletnev et al., 1982), and a high (1.6-Å) resolution X-ray structure of macromomycin has been described (Van Roey & Beerman, 1989). Apoactinoxanthin and macromomycin exhibit very similar tertiary structures: a seven-stranded antiparallel β-barrel domain linked to a smaller subdomain composed of two antiparallel β-sheet ribbons, with a large cleft formed by the interface of the barrel and ribbons.

Neocarzinostatin is the most thoroughly studied member of the antitumor chromoprotein family. NMR assignments and qualitative secondary structure analyses (Remerowski et al., 1990; Gao & Burkhart, 1991), a low-resolution NMR solution structure ensemble (Adjadj et al., 1992), and medium–high-resolution NMR solution structure ensembles (Gao et al., 1992) of aponeocarzinostatin have been determined. X-ray crystallographic structures of aponeocarzinostatin have been solved to resolutions of 1.8 Å (Kim et al., 1993) and 1.5 Å (Teplyakov et al., 1993). Aponeocarzinostatin has the same overall folding pattern as apoactinoxanthin and macromomycin. Recently, both high-resolution NMR (Tanaka et al., 1993) and X-ray (Kim et al., 1993) structures of the neocarzinostatin chromoprotein have been determined. The X-ray analysis (Kim et al., 1993) demonstrated that chromophore binding induces relatively small conformational changes, with only three residues showing C^α differences >1.0 Å. Both the solution and crystal structures reveal interactions between the chromophore and aromatic residues and the Cys37–Cys47 disulfide bridge that are likely to be involved in stabilizing the chromophore; however, some of the details of the interactions differ between the NMR and X-ray structures (Kim et al., 1993).

In this paper, we report the results of heteronuclear multidimensional NMR and molecular modeling studies of apokedarcidin. Sequential ^{1}H and ^{13}C assignments have been obtained for all residues, and ^{15}N assignments have been obtained for all residues excluding Ala1 and the four prolines. The backbone atom, $^1H^\beta$, and $^{13}C^\beta$ resonance assignments were obtained by a semiautomated analysis of six triple-resonance experiments (Friedrichs et al., 1994). Assignments for the side-chain resonances were obtained by interactive analysis of HCCH-COSY and HCCH-TOCSY spectra and analysis of additional experiments specific for aromatic rings and side-chain NH_2 groups. The results of secondary structure analysis and molecular modeling demonstrate that apokedarcidin has the same global folding topology as apoactinoxanthin, apomacromomycin, and aponeocarzinostatin. This is consistent with the sequence similarities (Figure 1). The resolution of the current NMR ensemble is sufficient to reveal details of the overall dimensions of the chromophore binding site and the general placement of side chains within the binding pocket. A comparison of the current NMR ensemble of apokedarcidin and the aponeocarzinostatin X-ray structure (Teplyakov et al., 1993) is presented. Differences that may allow kedarcidin to accommodate a chromophore that is significantly larger than that of neocarzinostatin (Edo et al., 1985; Leet et al., 1993) are noted. In addition, three potential proteolytic active sites are identified.

EXPERIMENTAL PROCEDURES

Sample Preparation. The kedarcidin chromoprotein was isolated from actinomycete strain L585-6 (ATCC 53650) (Lam et al., 1991; Hofstead et al., 1992; Leet et al., 1992). Growth conditions for strain ATCC 53650 have been described (Lam et al., 1991). In the present study, strain ATCC 53650 was first grown in the seed medium using [^{15}N]ammonium sulfate (0.25%) and [^{13}C$_6$]glucose (2%) as the sole nitrogen and carbon sources, supplemented with KH_2PO_4 (0.05%), $MgSO_4$ (0.1%), NaCl (0.05%), $CaCO_3$ (0.2%), and MOPS (0.44%, pH 7.0). After 72 h of incubation at 28 °C, the seed culture was inoculated into the production medium consisting of [^{13}C,^{15}N]celtone growth medium (Martek) supplemented with [^{13}C$_6$]glucose (0.5%). The production culture was further incubated at 28 °C for 72 h. The kedarcidin chromoprotein was isolated from the production culture as described previously (Hofstead et al., 1992; Leet et al., 1992). The apoprotein was prepared from the chromoprotein as described elsewhere (Zein et al., 1993b). Ultraviolet spectroscopy was used to determine the chromophore content of the sample. The sample was found to be greater than 15:1 apoprotein to chromoprotein. For the NMR sample, ^{13}C/^{15}N-labeled apokedarcidin (16.3 mg) was dissolved in 0.5 mL of 90% ^1H_2O/10% ^2H_2O buffer (pH 5.4) containing 36 mM deuterated sodium acetate. After transfer to a 5-mm NMR tube (Wilmad tube no. 535), the sample was degassed by application of a partial vacuum and refilling with argon gas. This procedure was repeated five times. The sample tube was then flame sealed.

NMR Data Acquisition and Processing: Two-Dimensional Experiments. All NMR experiments were performed using a three-channel Unity 600 spectrometer operating at a proton frequency of 599.91 MHz. The sample temperature was set to 20.0 °C for all experiments. Unless stated otherwise, experiments were collected using a proton-observe, carbon–nitrogen triple-resonance probe. In the heteronuclear experiments, the acquisition time in the proton-detected dimension was set between 55 and 65 ms for a spectral width of 7 kHz throughout. The proton carrier was set on resonance with the water frequency (4.84 ppm).

The 2D ^{15}N-edited HSQC spectrum (Figure 2) was acquired by collecting 256 complex points along t_1 for a ^{15}N spectral width of 1.6 kHz. Hypercomplex–TPPI sampling was employed at half-dwell intervals so that peaks folded an odd number of times are opposite in sign relative to unfolded peaks (e.g., ^{15}N–^{1}H cross-peaks of Val21 or Val76 in Figure 2). Solvent suppression was achieved by CW presaturation ($\gamma B_1 \sim 50$ Hz) during the entire 1.4-s relaxation delay.

A constant-time 2D ^{13}C-edited HSQC spectrum was collected with the ^{13}C carrier frequency set at 125 ppm. The interval between the ^{13}C excitation and read pulses was set to 13.4 ms ($1/^1J_{cc}$). Carbonyl decoupling during the t_1 evolution period was achieved by a cosine-modulated Hermite 180° pulse with one excitation band centered at 166 ppm. A total of 64 complex points were collected along t_1. The t_1 interferograms were apodized with a cosine function and then zero-filled to 256 points prior to Fourier transformation.

Two additional 2D ^{1}H,^{13}C-correlated experiments were recorded in order to confirm resonance assignments for the aromatic side chains: the recently published (H$^\beta$)C$^\beta$(C$^\gamma$C$^\delta$)-H$^\delta$ and the double relay (H$^\beta$)C$^\beta$(C$^\gamma$C$^\delta$C$^\epsilon$)H$^\epsilon$ experiments (Yamazaki et al., 1993). Both experiments were recorded with 40 complex points along t_1 for a spectral width of 5 kHz. A total of 512 transients were collected for each FID. The t_1 interferograms were extended to 80 complex points by linear prediction, apodized by a cosine squared function, and zero-filled to 256 points prior to Fourier transformation.

A series of *J*-modulated ^{15}N,^{1}H-COSY experiments were recorded to obtain estimates of $^3J_{\mathrm{NH}\alpha}$ coupling constants (Billeter et al., 1992). Each two-dimensional experiment in this series was collected with 128 complex points along t_1 for a ^{15}N spectral width of 1.6 kHz; 64 transients were collected for each FID. The following *J*-modulation delays were used: 8, 25, 40, 60, 80, and 100 ms. $^3J_{\mathrm{NH}\alpha}$ coupling constants were estimated from both cross-peak volumes and heights by nonlinear least-squares fitting. The interferograms were apodized with a 80°-shifted sine-bell function in t_1 and a 90°-shifted sine-bell function in t_2 prior to Fourier transformation.

NMR Data Acquisition and Processing: Three- and Four-Dimensional Experiments. Several heteronuclear 3D experiments were recorded. The following 3D experiments were utilized in the assignment of the backbone, C$^\beta$, and H$^\beta$ resonances: HNCACB, CBCA(CO)NH, HBHA(CO)NH, and HNHA(Gly).

The HNCACB experiment (Wittekind & Mueller, 1993) was acquired with 40 complex points along the ^{13}C t_1 dimension for a ^{13}C spectral width of 9 kHz. Along the ^{15}N t_2 dimension, 30 complex points were collected for a spectral width of 1.6 kHz. A total of 32 transients were collected for each FID. The ^{1}H rf field strengths were 37 and 5.7 kHz for hard rf pulses and MLEV decoupling, respectively. The ^{13}C rf field strength was set to 19.5 kHz for hard pulses, and the ^{15}N rf field was set to 7.3 kHz for hard pulses and 1.16 kHz for GARP1 decoupling. Carbonyl decoupling was achieved by cosine-modulated SEDUCE-1 decoupling with a peak rf field strength (sum of both sidebands) of 3.3 kHz (McCoy & Mueller, 1992a,b).

The CBCA(CO)NH and HBHA(CO)NH experiments were performed as proposed by Bax and co-workers (Grzesiek & Bax, 1993a). All spectral widths and frequency settings were identical to the ones used in the HNCACB experiment. In the CBCA(CO)NH experiment, 42 complex points were collected along the ^{13}C t_1 dimension and 30 complex points along the ^{15}N t_2 dimension. Frequency-shifted carbonyl pulses were employed in this experiment. On our spectrometer, the optimum phase of the last carbonyl 90° pulse was −51° instead of the reported +51° (Grzesiek & Bax, 1993a). In the HBHA(CO)NH experiment, 30 complex points were collected along the H$^\alpha$,H$^\beta$ t_1 dimension for a spectral width of 3.6 kHz, and 30 complex points were collected along the ^{15}N t_2 dimension for a spectral width of 1.6 kHz.

For the HNCACB, CBCA(CO)NH, and HBHA(CO)NH experiments, the ^{15}N t_2 interferograms were extended by 30 complex points using complex linear prediction (CLPD; Zhu & Bax, 1990). Along the ^{13}C dimension, resolution enhancement was achieved by inverse transformation of the F_1 dimension of the initial coarse spectra, inverse cosine apodization followed by 86 points of CLPD, cosine apodization of the extended FID, and finally reconstruction of the spectrum by Fourier transformation.

The HNHA(Gly) experiment (Wittekind et al., 1993) was collected with 44 complex points along t_1 (H$^\alpha$) and 32 complex points along t_2 (^{15}N) for spectral widths of 2 and 1.6 kHz, respectively. Here again, the t_1 and t_2 interferograms were extended by 44 and 32 complex points, respectively, using CLPD as described above. The extended time–domain data were zero-filled to 128 complex points in both dimensions prior to Fourier transformation. In all NH-correlated experiments, the time–domain data were zero-filled to 1024 complex points along t_3 prior to Fourier transformation. Zero-order baseline correction was applied along F_3 to remove any baseline offset. Only the downfield half of F_3 was stored on disk.

Through-bond connectivities between intraresidue and sequential NH and H$^\alpha$ resonances were determined with the 4D HNCAHA and HN(CO)CAHA experiments (Kay et al., 1992; Olejniczak, 1992). The optimized single-quantum versions (Olejniczak, 1992) were used. Spectral widths and number of time increments in the t_1 (C$^\alpha$), t_2 (H$^\alpha$), and t_3 (N) dimensions are as follows: 3 kHz, 10; 2 kHz, 10; 1.6 kHz, 20. The t_2 interferogram was recorded at half-dwell intervals. CO decoupling in the HNCAHA experiment was achieved using SEDUCE-1 (McCoy & Mueller, 1992a,b) with a peak rf field of 1.88 kHz. Frequency shifting of the SEDUCE-1 sequence was performed in the waveform generator. The sequence by Olejniczak et al. was modified by inserting a ^{1}H x, y purging pulse sandwich (durations of 5 and 3 ms, with an rf amplitude of 13 kHz) immediately following the t_2 evolution period, resulting in improved solvent peak suppression. In the HN(CO)CAHA experiment, the ^{13}C rf pulse amplitudes were adjusted for minimum excitation at a 18.3-kHz resonance offset ($\sim$C$^{\alpha}$, CO frequency difference). Frequency-shifted CO pulses were generated in the waveform generator. The 4D interferograms were Fourier transformed in the following manner. First, the t_1 and t_2 dimensions were apodized using a cosine function such that the last point in each FID was attenuated 10-fold and then zero-filled to 64 points prior to Fourier transformation. Next, the t_3 dimension was extended to 40 points by CLPD. Finally, the resolutions in the F_1 and F_2 dimensions were enhanced using the following procedure. The interferograms were reconstructed by inverse Fourier transformation followed by inverse cosine apodization. Next, the FIDs were extended 1-fold by mirror-imaged complex linear prediction (Zhu & Bax, 1990) followed by cosine apodization, zero-filling, and forward Fourier transformation. The final matrices consisted of 64 by 64 by 64 by 256 real points.

Resonance assignments in aliphatic side chains were determined using a modified version of the HCCH-COSY experiment (Kay et al., 1990), a gradient-enhanced HCCH-TOCSY experiment (Bax et al., 1990; Kay et al., 1993), and an NH$_2$-filtered variant of the CBCA(CO)NH experiment. Details regarding the latter experiment are given in the supplementary material. The HCCH-COSY experiment was modified in two ways. First, evolution of the ^{13}C coherence was achieved by a shifting ^{13}C echo pulse within a constant interval set to $1/(4^{1}J_{\mathrm{cc}})$. Second, water suppression was achieved by a combination of low-level water presaturation ($\gamma B_1 \sim 8$ Hz) and ^{1}H coherence purging: at the end of the COSY transfer, the ^{13}C magnetization is temporarily flipped along z. In the ensuing period, all ^{1}H coherence was suppressed by an x, y proton purging pulse sandwich. Subsequently, the ^{13}C magnetization is back-transferred to protons via reverse INEPT. The HCCH-COSY and HCCH-TOCSY spectra were acquired with 128 complex points in the ^{1}H evolution dimension (t_1) and 20 complex points placed at half-dwell intervals in the ^{13}C evolution dimension (t_2). The spectral widths in F_1 and F_2 were set to 7 and 3 kHz, respectively. A mixing time of 23 ms was used during the DIPSI-3 mixing sequence (Shaka et al., 1988) of the HCCH-TOCSY.

Carbon resonance assignments in aliphatic side chains were confirmed by the (H)C(CO)NH-TOCSY experiment (Logan et al., 1993; Montelione et al., 1993; Grzesiek et al., 1993). The version by Grzesiek et al. was used, although the sequence by Logan et al. gave similar results in test runs. A total of 42 and 32 complex points were collected along the ^{13}C (t_1) and ^{15}N (t_2) dimensions, respectively. The spectral widths were set to 7, 10, and 1.6 kHz in F_1, F_2, and F_3, respectively. ^{13}C pulse amplitudes were adjusted to the recommended values (Grzesiek et al., 1993), and all carbonyl pulses were frequency shifted in the waveform generator. The ^{15}N 90° pulse was 37.5 μs, and the ^{1}H MLEV decoupling field strength was 5.9 kHz. The DIPSI-3 mixing time was 15 ms ($\gamma B_1 = 7.24$ kHz).

Qualitative estimates of heteronuclear $^{3}J_{\mathrm{H}\beta\mathrm{N}}$ coupling constants were obtained from a HNHB spectrum (Archer et al., 1991). This spectrum was recorded with 32 complex points along the ^{15}N t_1 dimension and 64 points along the H$^{\beta}$ t_2 dimension for spectral widths of 1.6 and 5 kHz. Again, the t_2 interferograms were extended by 32 complex points using CLPD. Resolution enhancement in F_1 was obtained by inverse Fourier transformation of the coarse spectrum followed by CLPD on the reconstructed t_1 interferogram and subsequent forward Fourier transformation. The final 3D matrix consisted of 128 by 256 by 512 real points.

Estimates of homonuclear J-couplings between vicinal proton pairs were obtained from gradient-enhanced ^{13}C- and ^{15}N-edited 3D ^{1}H–^{1}H HSQC-TOCSY experiments (L. Mueller, unpublished). In these experiments, proton magnetization evolves in t_1 followed by an INEPT transfer to either ^{13}C or ^{15}N via one-bond heteronuclear couplings. After the t_2 evolution period, the ^{13}C or ^{15}N coherence is dephased by a strong z-gradient pulse. The dephased magnetization is then back-transferred to protons by a reverse INEPT. This is followed by ^{1}H–^{1}H mixing with a clean-MLEV pulse train of short duration ($\tau_{\mathrm{m}} < 16$ ms). Finally, a coherence transfer echo is induced by another gradient pulse. Qualitative estimates of $^{3}J_{\mathrm{HH}}$ are extracted from peak intensities (Constantine et al., 1994a). The gradient-enhanced HSQC-TOCSY spectrum was recorded with 128 complex points in t_1 (^{1}H) for a spectral width of 7 kHz and 16 complex points in t_2 (^{13}C) for a spectral width of 4 kHz. The t_2 interferograms were extended by 16 complex points using mirror-imaged CLPD. The final 3D matrix consisted of 256 by 128 by 1024 real points. The gradient-enhanced ^{15}N-edited spectrum was obtained with 128 complex points along t_1 and 32 points along t_2 for spectral widths of 7 and 1.6 kHz, respectively. The final ^{15}N-edited HSQC-TOCSY 3D spectral matrix was 256 by 128 by 1024 real points. Resolution enhancement along the ^{15}N dimension again was achieved by doubling the length of the t_2 interferograms using complex linear prediction.

Two ^{15}N-edited 3D NOESY spectra ($\tau_{\mathrm{m}} = 50$ and 100 ms) and one ^{13}C-edited 3D NOESY spectrum ($\tau_{\mathrm{m}} = 70$ ms) were recorded using gradient-enhanced pulse sequences. The details of these sequences are given in the supplementary material.

Homology Modeling. An initial model of apokedarcidin was constructed on the basis of the sequence homology between kedarcidin and neocarzinostatin (Figure 1) using the program CONGEN (Bruccoleri & Karplus, 1987; Bruccoleri et al., 1988; Bruccoleri, 1990, 1993). Using the hydrogen construction algorithm from CHARMM, version 16 (Brooks et al., 1983), polar hydrogens were added to the 1.5-Å resolution X-ray structure of aponeocarzinostatin (Teplyakov et al., 1993), and these hydrogens were then minimized for 500 steps of adopted-basis Newton–Raphson (ABNR) minimization (Brooks et al., 1983). Next, 250 steps of ABNR minimization were applied to the structure with harmonic constraints of 20 kcal mol^{-1} Å^{-2} applied to all atoms. Mutations, insertions, and deletions (Figure 1) were made using the CONGEN SPLICE command to generate the kedarcidin sequence from neocarzinostatin while maintaining the homologous backbone coordinates. The manner in which changes were incorporated was decided by visual inspection. This allowed identification of loops and strands to be regenerated using a complete conformational search versus simple side-chain substitutions. Five such loops (residues 26–30, 41–45, 58–62, 76–81, and 89–94) were identified that had either large sequence changes, insertions or deletions, or substitutions involving a glycine or proline. One β-strand (residues 104–108) with a bulge was also selected for a complete search because of a deletion in the sequence.

With the identification of regions to be rebuilt, the next step in the modeling was a single CONGEN run to reconstruct individual mutated side chains. The iterative side-chain construction algorithm was executed over residues 2, 5, 6, 8, 11, 18, 20, 22, 24, 31, 33, 35, 39, 40, 48, 49, 51, 53, 54, 55, 56, 57, 63, 66, 67, 73, 75, 82, 83, 87, 96, 97, 98, 99, 102, and 103 using a torsion angle grid of 30°. Next, loops 26–30 and 58–62 were searched simultaneously using a 30° backbone grid and a torsion energy minimum periodicity grid for the side chains. A simultaneous search was used to allow for mutual interactions between these two spatially adjacent loops. The remaining four regions were searched in the order 41–48, 76–81, 89–94, and 104–108. All side-chain searches were performed using van der Waals avoidance (Bruccoleri, 1993) with an energy cutoff of 5 kcal/mol. The CONGEN calculations were performed on a SGI Onyx workstation with 150-MHz R4400 processors. The resulting apokedarcidin model has a backbone atom RMSD to aponeocarzinostatin over the aligned residue positions (Figure 1) of 1.28 Å.

Constraint Derivation and Solution Structure Determination. Backbone ϕ dihedral constraints were derived from $^3J_{\alpha NH}$ coupling constants. The ϕ dihedral angles were constrained to $-120 \pm 40°$ when the $^3J_{\alpha NH}$ exceeded 8.5 Hz and to $-120 \pm 50°$ when $^3J_{\alpha NH}$ was between 7.5 and 8.5 Hz. In cases of $^3J_{\alpha NH} < 5.0$ Hz, the ϕ angles were constrained to $-50 \pm 40°$.

Stereospecific H^β, Val γ-methyl, and Leu δ-methyl assignments, as well as constraints on χ^1 and Leu χ^2 side-chain dihedral angles, were obtained from analysis of peak intensity patterns in the 3D NOESY, HNHB, and short mixing time ^{13}C-edited HSQC-TOCSY spectra (Constantine et al., 1994a). In cases where the data indicated one predominant χ^1 or Leu χ^2 rotamer ($\sim$60°, $\sim$–60°, or $\sim$180°), the dihedral angle was constrained to be within 40° of the indicated staggered conformation. In some cases, it was only possible to exclude one of the three favored rotamers.

Cross-peaks in the 3D NOESY spectra were assigned in a semiautomated, iterative manner. Initially, all unambiguous NOEs were assigned. The initial unambiguous NOEs were used to derive an initial constraint set for input to the X-PLOR program (Brünger, 1992). A simulated annealing protocol (Nilges et al., 1988), with the high-temperature phase temperature set to 600 K and with electrostatics, empirical dihedral angle, and attractive van der Waals terms excluded, was used with the initial constraints to generate nine different preliminary apokedarcidin solution structures starting from the CONGEN-built model. This was accomplished by varying the initial velocity random number seed. The preliminary structure set was then searched (Kline et al., 1990) in an automated manner to assign additional NOE cross-peaks, producing the final constraint list used to determine the reported structures.

The NOEs were converted to proton–proton distance constraints by comparing the measured cross-peak volumes to calibration volumes. Backbone–backbone NOEs within the identified β-sheet regions were used to establish calibration volumes by referring to the standard distance ranges for these interactions (Wüthrich, 1986). NOEs were conservatively classified into very strong, strong, medium, and weak NOE bins, corresponding to upper-bound proton–proton distance constraints of 2.5, 3.0, 4.0, and 5.0 Å, respectively.

After the final constraint list was obtained, models of the apokedarcidin solution structure were generated with the variable target function program DIANA (Güntert et al., 1991). NOE distance constraints were entered as upper distance bounds only (i.e., lower bounds were set to the sum of the van der Waals radii), and pseudoatoms with appropriate distance corrections (Wüthrich et al., 1983) were used for equivalent and nonstereospecifically assigned protons. Automated stereoassignment was not employed; only the stereospecific assignments derived from direct inspection of the NMR data (Constantine et al., 1994a) were used. Structures were generated using two cycles of the REDAC strategy (Güntert & Wüthrich, 1991) using the standard minimization parameters (Güntert, 1992), with the exception that the local target function acceptance cutoff for generating redundant constraints was increased from 0.4 to 0.6 Å^2. Accepted DIANA structures were subjected to a simulated annealing/energy minimization protocol (Nilges et al., 1988) using the X-PLOR program (Brünger, 1992), which we briefly describe. An initial 1000-step restrained Powell minimization was followed by 16 ps of high-temperature (600 or 800 K) molecular dynamics using the "soft-square" NOE potential (Brünger, 1992). The NOE potential was then converted to a full harmonic square-well function, and the temperature was gradually lowered to 300 K. This was followed by a final 2000 steps of restrained Powell minimization. A time step of 1 fs was used for the molecular dynamics calculations. Instead of using pseudoatoms, distance constraints involving equivalent and nonstereospecifically assigned protons were incorporated as $(\sum r^{-6})^{-1/6}$ effective distances (Constantine et al., 1992, 1994b). This approach allows the use of tighter constraints, and it is expected to produce conformations that more closely reflect the observed NOEs than those produced using pseudoatoms. Experimental constraints and harmonic bond length and bond angle terms were included in all minimization and dynamics steps using the X-PLOR parallhsa.pro parameter set. Electrostatics, attractive van der Waals, and empirical dihedral angle functions were excluded. X-PLOR calculations were performed on either a Silicon Graphics 4D/440 VGX computer or a CRAY YMP2 supercomputer. Molecular graphics analysis was performed with the Insight II program (Biosym Technologies). Characterization of the stereochemical quality of the structures was accomplished with analysis facilities provided in X-PLOR and with the PROCHECK program (Laskowski et al., 1993).

RESULTS AND DISCUSSION

Sequential Assignments. Figure 2 shows a 2D ^{1}H–^{15}N HSQC spectrum of apokedarcidin. The cross-peaks are labeled with their assignments. The backbone assignments were obtained in a semiautomated fashion (Friedrichs et al., 1994). Briefly, lists of picked cross-peaks from the 3D HNCACB, 3D CBCA(CO)NH, 3D HNHA(Gly), 3D HBHA(CO)NH, 4D HNCAHA, and 4D HN(CO)CAHA experiments were used as input to the automation algorithm. The program groups peaks from the different spectra on the basis of their amide ^{1}H and ^{15}N chemical shifts and classifies the peaks as arising from either intra- or interresidue $^{13}C^\alpha$, $^{13}C^\beta$, $^1H^\alpha$, or $^1H^\beta$ resonances. The program then links the groups by matching sequential connectivities involving $^1H^\alpha$, $^{13}C^\alpha$, and $^{13}C^\beta$ resonances. The final stage of the semiautomated assignment process involves aligning segments of linked groups with the protein sequence by matching the $^{13}C^\alpha$ and $^{13}C^\beta$ chemical shift profiles of the linked groups with the profile predicted by kedarcidin's primary sequence. Details of the assignment algorithm and its application to apokedarcidin are provided elsewhere (Freidrichs et al., 1994).

During the assignment procedure, it became clear that there were a number of extra spin systems represented by relatively

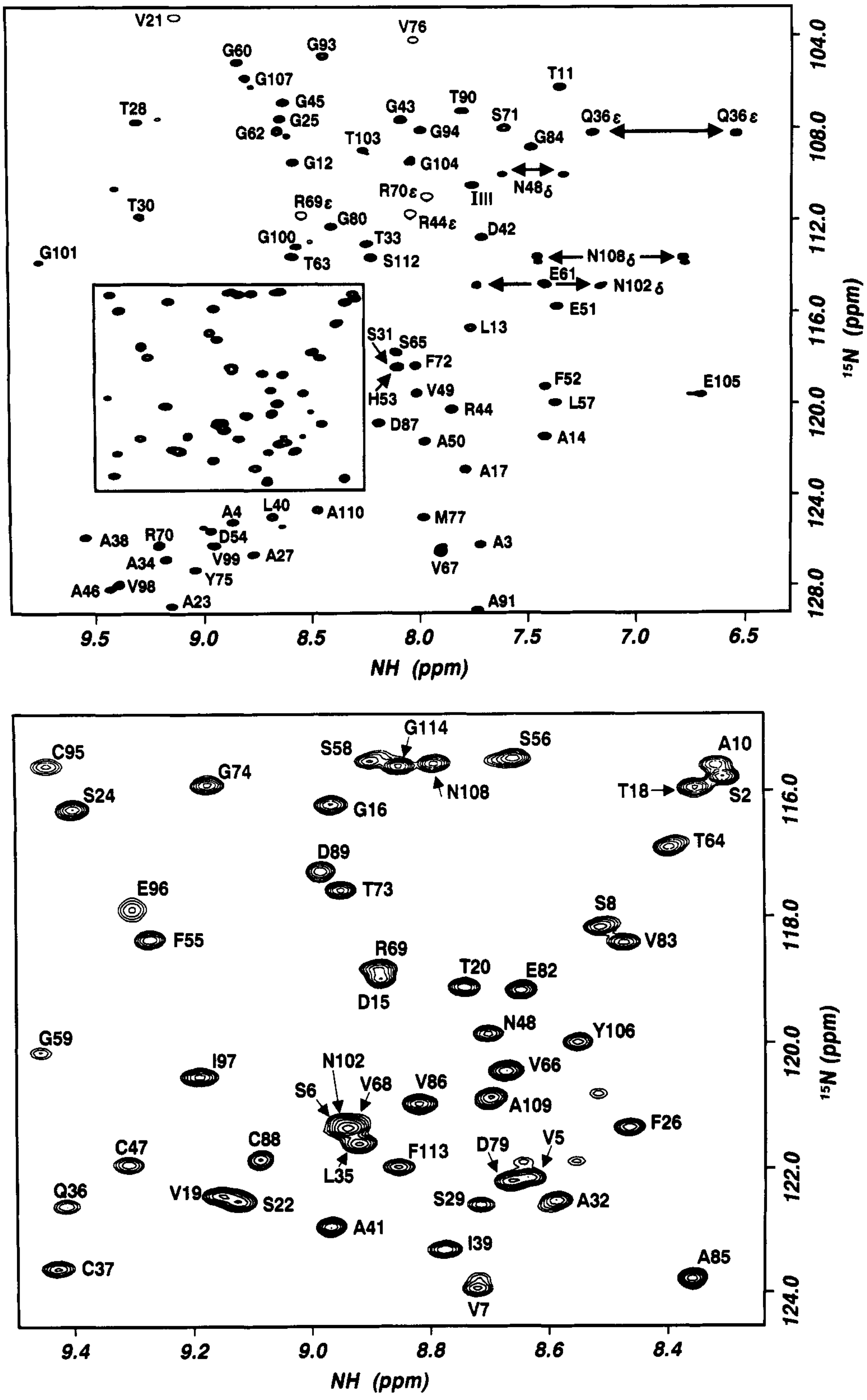

FIGURE 2: 600-MHz 2D ^{1}H–^{15}N HSQC spectrum of apokedarcidin. Backbone and side-chain ^{1}H–^{15}N cross-peaks are labeled. The boxed cross-peaks in the full HSQC spectrum (panel A, top) are shown expanded in panel B (bottom). Folded cross-peaks are plotted with only two contour levels.

weak cross-peaks among the different spectra. These cross-peaks were included in the analysis described above and resulted in a set of parallel assignments for segments Phe26–Thr28, Asp54–Phe55, and Glu105–Asn108 of the protein. These assignments are attributed to contamination of the apokedarcidin preparation by residual chromoprotein, which was estimated to be present at approximately 6% as determined by ultraviolet spectroscopy. As described below, the latter two segments flank the chromophore binding pocket.

All four cysteine residues of apokedarcidin have downfield-shifted $^{13}C^{\beta}$ resonances (Cys37 at 50.5 ppm, Cys47 at 47.7 ppm, Cys88 at 39.9 ppm, and Cys95 at 46.7 ppm). This type of shift indicates that these cysteine residues are involved in disulfide bonds, as has been seen with other proteins that

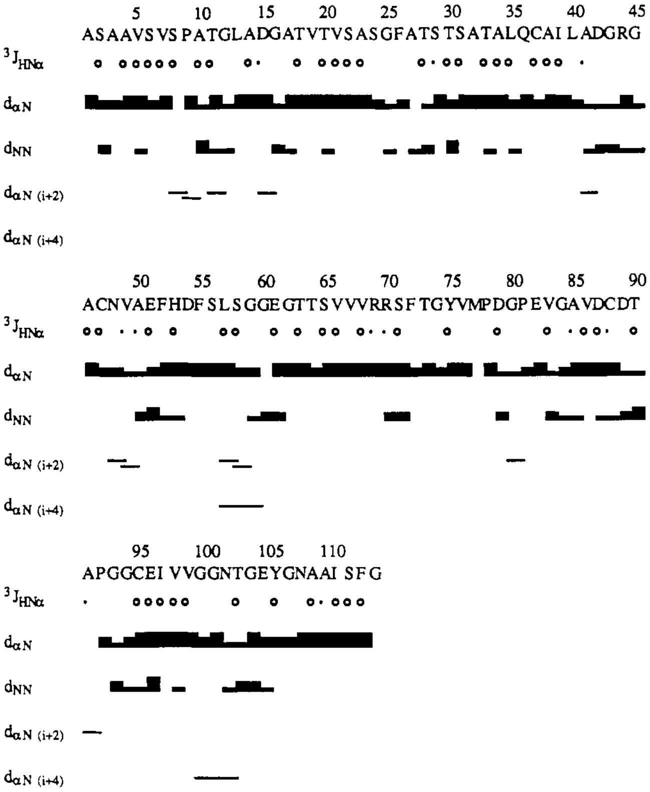

FIGURE 3: Summary of the sequential and medium-range backbone–backbone NOEs observed for apokedarcidin. Strong, medium, and weak sequential NOEs are distinguished by thick, medium, and thin solid horizontal bars between adjacent residues, respectively. Medium-range NOE connectivities are indicated by thin horizontal lines. $^3J_{\alpha NH} < 5.0$ Hz and $^3J_{\alpha NH} > 7.5$ Hz are indicated by small filled and large open circles, respectively.

form cysteine disulfides for which ^{13}C assignments are available (Hansen, 1991; Constantine et al., 1993). This result is expected, since the corresponding cysteines in the related structure of neocarzinostatin form disulfides (Kim et al., 1993; Teplyakov et al., 1993). After the backbone, $^1H^\beta$, and $^{13}C^\beta$ assignments were completed, side-chain assignments were obtained primarily from an analysis of HCCH-COSY and HCCH-TOCSY spectra (Clore et al., 1990; Constantine et al., 1993). This analysis also served to confirm the sequential assignments obtained by the semiautomated assignment procedure. The resonance assignments are available as supplementary material (Table S-1).

Qualitative Secondary Structure Analysis. As described above, the sequential resonance assignments obtained for apokedarcidin were based on observed scalar connectivities, most of which are essentially independent of local conformations. On the other hand, NOE connectivities are rich in conformational information (Wüthrich, 1986). Summaries of the observed sequential and medium-range backbone–backbone NOEs, as well as the locations of residues with $^3J_{\alpha NH} < 5.0$ Hz or $^3J_{\alpha NH} > 7.5$ Hz, are presented in Figure 3. Residues with strong $d_{\alpha N}$ sequential connectivities and/or with $^3J_{\alpha NH} > 7.5$ Hz predominate, indicating that the regular secondary structure of apokedarcidin is composed primarily of β-strands. Unbroken stretches of strong or very strong $d_{\alpha N}$ sequential connectivities are observed for residues 1–8, 13–16, 17–25, 29–41, 51–60, 61–77, 84–89, 94–101, and 104–113. Fifty-two residues have $^3J_{\alpha NH} > 7.5$ Hz, whereas only 11 have $^3J_{\alpha NH} < 5.0$ Hz. The small $^3J_{\alpha NH}$ coupling constants, and the sequential d_{NN} and medium-range NOE connectivities, indicate that bends, turns, or loop conformations occur in the vicinities of residues 8–11 (which include *cis*-Pro9), 14–17, 41–43, 48–52, 57–61, 69–71, 76–82 (which include *cis*-Pro81), 88–93, and 100–105.

Deviations of $^{13}C^\alpha$ and $^{13}C^\beta$ chemical shifts from random coil values (Spera & Bax, 1991) are known to correlate with local polypeptide backbone conformations (Spera & Bax, 1991; Wishart et al., 1991; Fairbrother et al., 1992; Wittekind et al., 1992; Constantine et al., 1993; Metzler et al., 1993). The $^{13}C^\alpha$ resonances tend to shift upfield in extended (β-strand) conformations and downfield in helices. The $^{13}C^\beta$ resonances display the opposite trends. Panels A and B of Figure 4 display deviations from random coil values for the apokedarcidin $^{13}C^\alpha$ and $^{13}C^\beta$ resonances, respectively. Enhanced deviations (Metzler et al., 1993), obtained by subtracking the $^{13}C^\beta$ deviations from the $^{13}C^\alpha$ deviations, are displayed in Figure 4C, and enhanced and smoothed deviations (Metzler et al., 1993) are shown in Figure 4D. Examination of the data presented in Figure 4 reveals that the protein is composed primarily of extended strands. This is especially clear in panels C and D of Figure 4, which are dominated by negative deviations. These results are generally consistent with the local conformations indicated by the $^3J_{\alpha NH}$ coupling constants and the sequential and medium-range NOE information (Figure 3).

The above analysis clearly indicates that apokedarcidin is predominantly a β-sheet protein, as expected on the basis of the sequence similarities to macromomycin, actinoxanthin, and neocarzinostatin (Figure 1). In order to further delineate the β-strands and their organization into β-sheets, long-range backbone–backbone NOEs must be examined. Figure 5 schematically depicts the backbone–backbone NOE connectivities which define the apokedarcidin secondary structure. Ten β-strands, designated A–J, have been identified. A three-stranded antiparallel β-sheet, composed of β-strands A, B, and F, is illustrated in Figure 5A. Figure 5A also depicts parallel contacts between the C-terminal portion of strand J (residues 112–114) and residues 11–13. The latter residues apparently do not adopt a regular extended conformation. Figure 5B shows a four-stranded antiparallel β-sheet formed by the N-terminal half of β-strand C, β-strand E, β-strand I, and the N-terminal portion of β-strand J. A two-stranded antiparallel β-sheet hairpin, formed by β-strand D and the C-terminal half of β-strand C, is also shown in Figure 5B. Finally, Figure 5C depicts a two-stranded antiparallel β-sheet hairpin formed by β-strands G and H. This qualitative description of apokedarcidin's β-sheet structure is very similar to those previously reported for aponeocarzinostatin (Remerowski et al., 1990; Gao & Burkhart, 1991), indicating that apokedarcidin's tertiary fold should also be similar. The remainder of this report focuses on the three-dimensional structure of apokedarcidin.

Solution Structure Determination. Analysis of the ^1H–^{15}N *J*-modulated COSY data yielded 63 backbone ϕ dihedral angle constraints. Inspection of intraresidue NOEs and peak intensities in the HNHB and ^{13}C-edited HSQC-TOCSY spectra afforded 47 χ^1 and 2 Leu χ^2 side-chain dihedral angle contraints (Table S-2). These data also yielded stereospecific assignments for 9 Val γ-methyl pairs, 2 Leu δ-methyl pairs, and 34 H^β methylene proton pairs, as reported in the supplementary material (Table S-1).

An initial analysis of the 3D NOESY spectra afforded 279 sequential distance constraints, 40 medium-range distance constraints, and 111 long-range distance constraints. (Intraresidue distance constraints were not used in the preliminary modeling stage.) The distance constraints, along with the

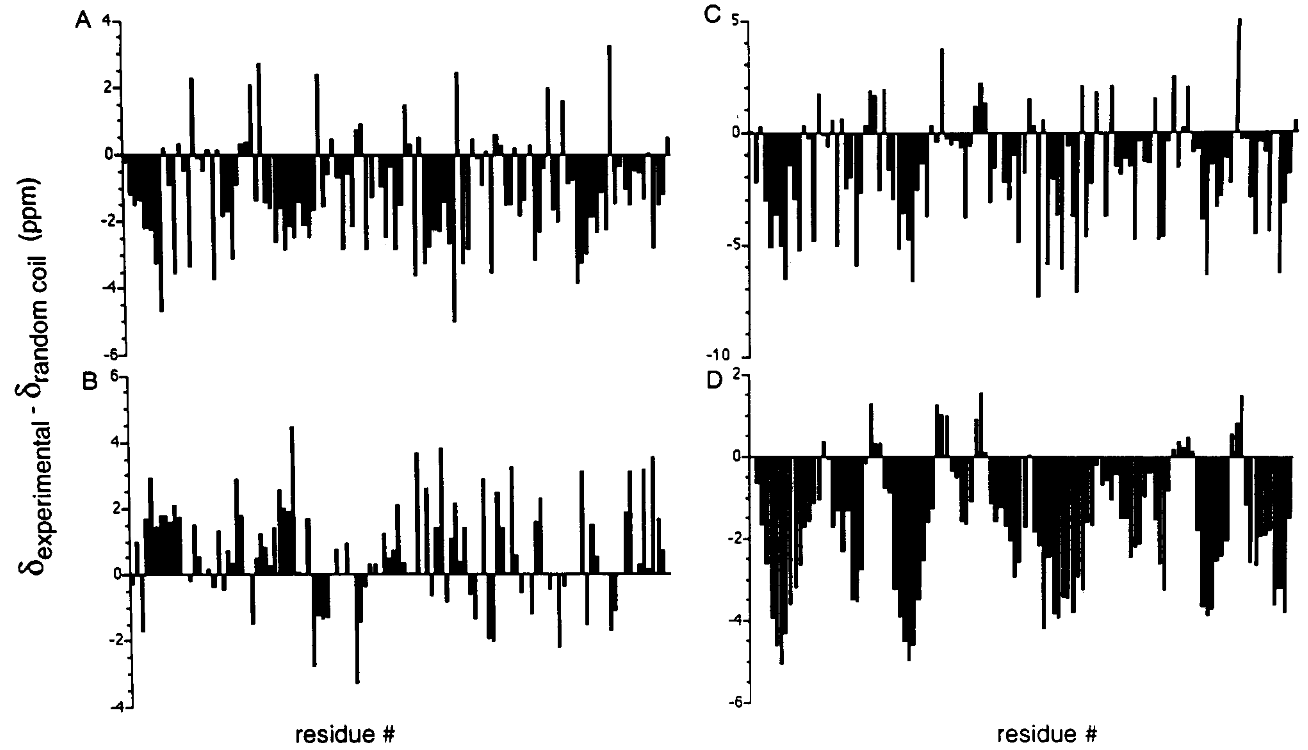

FIGURE 4: Histograms showing the deviations of the apokedarcidin ^{13}C chemical shifts, defined as the measured ^{13}C chemical shift minus the random coil ^{13}C chemical shift (Spera & Bax, 1991). (A) $^{13}C^{\alpha}$ deviations. His residues are excluded (values set to 0 ppm). (B) $^{13}C^{\beta}$ deviations. His and Cys residues are excluded. (C) Enhanced deviations (Metzler et al., 1993), obtained by subtracting the $^{13}C^{\beta}$ deviations from the $^{13}C^{\alpha}$ deviations. (D) Enhanced and smoothed deviations (Metzler et al., 1993), obtained by application of a three-point smoothing function to the enhanced deviations. Helix-like and extended regions are indicated by positive and negative peaks, respectively, in panels C and D.

112 dihedral angle constraints, were used to generate nine preliminary models of the apokedarcidin solution structure. These were produced by using the initial CONGEN-built model (see Experimental Procedures) as a starting structure for simulated annealing runs. Different random number seeds were used to generate different initial velocities for each run. The nine preliminary structures have an average backbone (N, C, and C^{α}) atom RMSD to the mean structure of 0.87 Å over all residues, and the backbone atom RMSD between the mean structure and the CONGEN-built model is 2.80 Å. The set of nine preliminary structures was searched in an automated manner (Constantine et al., 1994b) to assign additional NOE cross-peaks, yielding a final set of 785 distance constraints containing 242 intraresidue constraints, 292 sequential constraints, 56 medium-range constraints, and 195 long-range constraints. All of the derived distance constraints are available as supplementary material (Table S-3).

The DIANA program (Güntert et al., 1991) was used to generate a set of 80 (initially random) models of apokedarcidin using the final constraint list. After two cycles of REDAC (Güntert & Wüthrich, 1991; Güntert, 1992), the best structure in the set had a DIANA target function value of 1.76 Å^2 and a maximum violation of 0.35 Å. Of the 80 structures, 11 were selected for further refinement using the criteria that no distance constraint violations >0.60 Å were present and the target function value was <6.0 Å^2.

Relatively few acceptable structures were generated by the DIANA run. Distance constraint violations are distributed throughout the nonconverged structures, with long-range constraints and constraints within the exposed loop and turn regions (see below) showing a higher tendency for being violated. It is well-known that the variables target function approach encounters sampling difficulties with β-sheet proteins, particularly when the number of experimental constraints is low (Güntert, 1992). The current number of experimental constraints for apokedarcidin is relatively low (~8 constraints/residue). This is due to the fact that no data on a ^2H_2O sample have yet been acquired, and a number of cross-peaks in the 3D NOESY data are currently unassigned due to ambiguities. Analysis of 4D NOESY data will yield additional NOE cross-peak assignments (in progress).

Since the number of acceptable structures generated by the first DIANA run was rather low, a second run of 80 structures was performed, again using two cycles of REDAC. From this run, 17 acceptable structures were generated, yielding a set of 28 accepted DIANA structures in total. The resolution of the DIANA structure set is low, with average backbone atom and all heavy atom RMSDs between the individual structures and the mean coordinates of 1.72 ± 0.26 and 2.20 ± 0.22 Å, respectively. As demonstrated below, much higher resolution is obtained *via* simulated annealing refinement using $(\sum r^{-6})^{-1/6}$ effective distances. This approach affords tighter constraints than pseudoatom center averaging.

The first attempt to refine 28 accepted DIANA structures by X-PLOR simulated annealing was performed with the high-temperature phase temperature set to 600 K and the NOE constraint force constant set to 50 kcal mol^{-1} Å^{-2}. Of the 28 DIANA structures, only three achieved an acceptable level of refinement, i.e., with no distance constraint violations >0.7 Å and with a total RMS distance constaint violation <0.10 Å. Two of these three accepted structures had no violations >0.5 Å. These results indicate that there are no intrinsic problems with the constraints themselves, since adequate constraint satisfaction can be achieved. However, the conformational sampling properties of the original annealing protocol appear to be such that a sufficient level of constraint

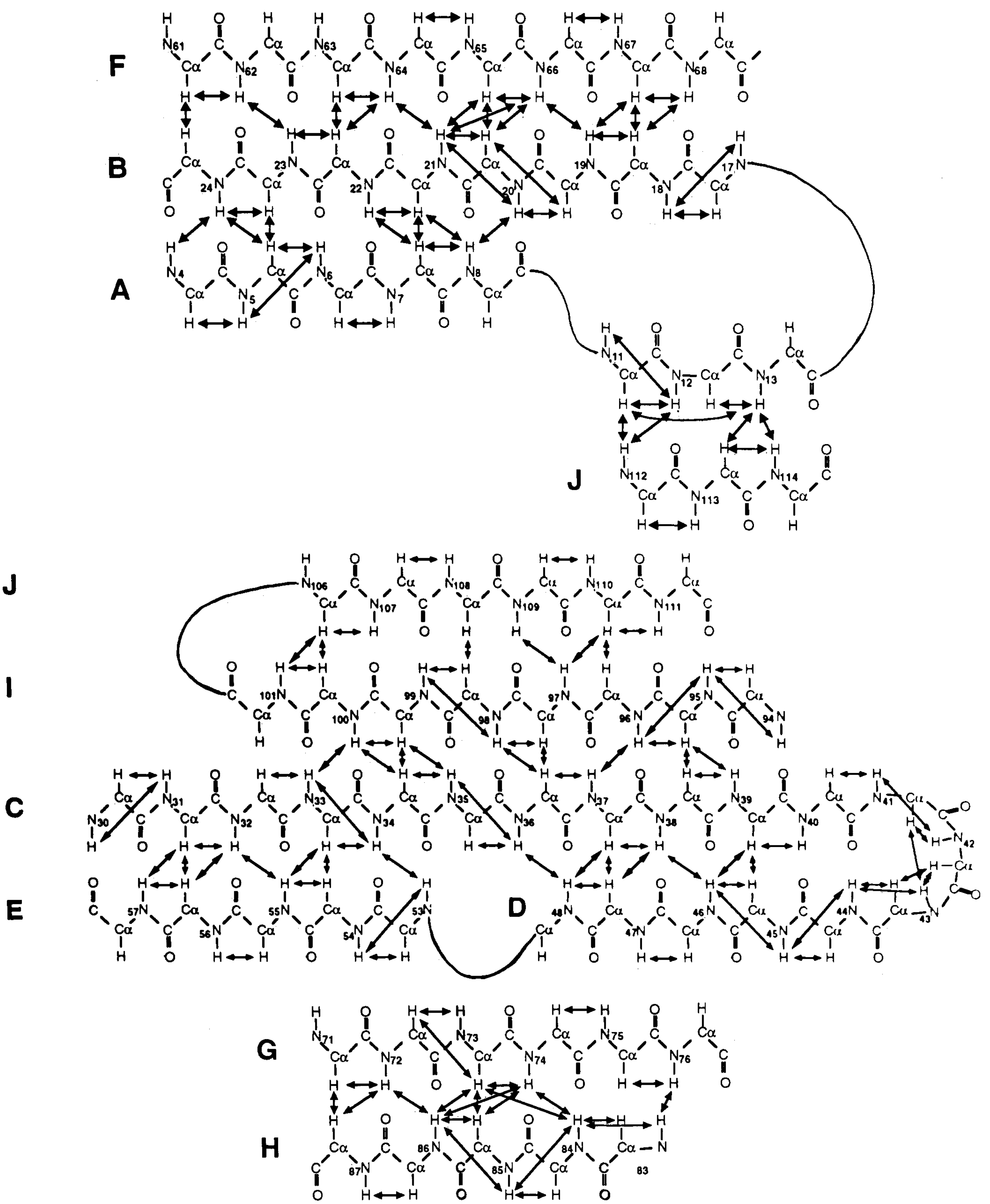

FIGURE 5: Schematic diagrams illustrating sequential, medium-range, and long-range NOE connectivities defining apokedarcidin β-sheets. (A, top) NOEs among β-strands A, B, and F. Interactions involving the C-terminal portion of β-strand J and residues 11–13 are also shown. (B, middle) NOEs involving β-strands C, D, E, I, and J. (C, bottom) NOEs between β-strands G and H.

satisfaction is achieved only rarely. Therefore, the remaining 25 DIANA structures were subjected to a modified simulated annealing protocol with the high-temperature phase temperature set to 800 K and the NOE constraint force constant set to 60 kcal mol^{-1} Å^{-2}. An additional 12 structures with adequate constraint satisfication were obtained from this run, resulting in a final set of 15 apokedarcidin solution structure models.

The average backbone atom and all heavy atom RMSDs between the individual structures and the mean coordinates are 0.68 ± 0.08 and 1.08 ± 0.11 Å, respectively. Over 82 residues in the well-defined regions (residues 4–25, 34–52,

Table 1: Structural Statistics for the 15 X-PLOR-Refined Apokedarcidin Structures

⟨backbone N, C, and C$^{\alpha}$ atom RMSD to mean⟩	0.68 ± 0.08 Å
⟨all heavy atom RMSD to mean⟩	1.08 ± 0.11 Å
⟨RMS distance constraint violation⟩	0.094 ± 0.004 Å
⟨no. of distance constraint violations > 0.5 Å⟩	1.4 ± 1.1
⟨no. of distance constraint violations > 0.3 Å⟩	22.0 ± 3.3
⟨RMS dihedral angle constraint violation⟩	0.08 ± 0.01°
⟨bond length deviation from ideality⟩	0.026 ± 0.001 Å
⟨bond angle deviation from ideality⟩	2.87 ± 0.02°
⟨improper torsion deviation from ideality⟩	1.55 ± 0.02°

61–76, 84–101, and 108–114), the average backbone atom RMSD between the individual structures and the mean coordinates is 0.39 ± 0.06 Å. This represents a very substantial increase in resolution over the original DIANA structures. Large increases in structural resolution resulting from the use of simulated annealing with effective distances in place of pseudoatoms have been reported for other proteins (Schwabe et al., 1993; Constantine et al., 1992, 1994b). The mean NMR structure has backbone atom RMSDs of 2.72 and 2.80 Å, respectively, to the aponeocarzinostatin X-ray structure (Teplyakov et al., 1993) and the original CONGEN-built model of apokedarcidin. These relatively large differences indicate that the NMR structures are not unduly biased by the initial models.

Additional structural statistics are reported in Table 1. All dihedral angle constraints are satisfied very well. The residual distance constraint violations are moderately high, with an average of 1.4 violations per structure between 0.5 and 0.7 Å. Since, as discussed above, the current number of NOE constraints is relatively low, these violations most likely reflect sampling difficulties. The bond length and bond angle deviations from ideal values (those in the X-PLOR parallhsa.pro parameter set) are moderately high, reflecting mild distortions induced by the residual constraint violations. The stereochemical quality of all 15 structures was also examined using PROCHECK (Laskowski et al., 1993). On average, 78% of the residues fall in the most favored regions of the Ramachandran map, 21% fall within the moderately or marginally allowed regions, and 1% fall in the disfavored regions. No residues are found consistently in the disfavored regions. The residues that occur most frequently in the disfavored regions are Asp54, Met77, and Glu105, each of which is in the disfavored regions in three structures. These residues are all in relatively disordered parts of the structures (see below). The planarity and chirality restrictions are satisfied very well by all structures, and the number of bad contacts found is only 1 per structure.

Overall Fold and Local Backbone Conformations. Two views of the superimposed polypeptide backbones of the 15 refined apokedarcidin models are presented in panels A and B of Figure 6. Figure 6B also includes the backbone of aponeocarzinostatin (heavy red trace), derived from the X-ray coordinates (Teplyakov et al., 1993). The seven-stranded antiparallel β-barrel is apparent in Figure 6A, which presents a "frontal" view of the protein, i.e., a view looking into the chromophore binding pocket. In general, the β-strands are well-defined, with higher disorder observed for the exposed loops and turns. The local structural precision is further characterized by the data presented in Figure 7, which shows residue-specific RMS displacements of the apokedarcidin models from the mean coordinates for the backbone N, C, and C$^{\alpha}$ atoms (heavy trace) and side-chain heavy atoms (thin trace). Regions displaying relatively high backbone disorder include residues 1–3, 26–28, 53–55, 58–59, 77–82, and 102–105.

A schematic ribbon drawing of structure 8 is shown in Figure 8. This structure was chosen as the representative structure for the set, since it is the individual structure with the lowest backbone atom and all heavy atom RMSDs to the mean coordinates. These values are 0.52 and 0.89 Å, respectively. Also, structure 8 is one of the better models in terms of constraint satisfication, with an RMS distance constraint violation of 0.088 Å. The ribbon diagram shown in Figure 8 is intended to serve as a convenient reference for the detailed description of the protein's backbone conformation given in the following paragraph.

Kedarcidin's N-terminal tail (residues 1–3) is disordered. This is followed by β-strand A (residues 4–8), which lies on the back side of the protein in the view of Figure 6A. β-Strand A is terminated by a type VIb bend (Richardson & Richardson, 1989) involving *cis*-Pro9 (ψ = 155.8 ± 5.1°) and Ala10. Residues 11–14 compose an irregular but well-defined loop on the back side of the protein, followed by a type II turn (residues 15 and 16) and β-strand B (residues 17–25), which also lie on the back side. Residues 26–29 form an irregular and somewhat disordered loop at the top of the protein. β-Strand C (residues 30–40) lines the central region of the chromophore binding site. The C-terminal protion of β-strand C pairs with β-strand D, forming a distorted β-hairpin at the base of the binding pocket. A type I turn (residues 41–42) connects β-strands C and D. Residues 49–52 are involved in a type III (helix-like) turn that leads into β-strand E (residues 53–57), which flanks the binding pocket. A distorted type I-like turn at the top of the protein is formed by residues 58–60. This region accommodates a one-residue deletion relative to the neocarzinostatin sequence (Figure 1). The 58–60 turn is followed by β-strand F (residues 61–68) on the back side. Residues 69 and 70 form a bend leading into (distorted) β-strand G (residues 71–76). Residues 77–82 compose an irregular loop which forms the "lower lip" of the binding pocket. This region accommodates a one-residue insertion relative to the neocarzinostatin sequence (Figure 1). Within the 77–82 loop, *cis*-Pro81 adopts a type VIb bend-like conformation (ψ = 153.1 ± 42.3°). The distorted β-strand H (residues 83–87) pairs with β-strand G. Residues 88–91 form a type III turn that is immediately followed by a type I turn (residues 92–93) at the base of the binding site. β-Strand I (residues 94–101) lies adjacent to β-strand C in the central region of the binding pocket. Residues Gly93 and Gly94 represent a two-residue insertion relative to the neocarzinostatin sequence (Figure 1). Residues 102–105 are somewhat disordered, with residues 102 and 103 involved in a type I turn that forms the "upper lip" of the binding pocket. Finally, residues 106–114 form β-strand F, which flanks the binding pocket. β-Strand F accommodates a one-residue deletion relative to the neocarzinostatin sequence (Figure 1).

Side-Chain Conformations and Binding Site Structure. The primary sequence of apokedarcidin (Figure 1) contains unusually high proportions of certain residue types. There are 18 alanine, 18 glycine, 12 serine, 11 threonine, and 13 valine residues. It is also a highly acidic protein, containing 6 aspartate and 5 glutamate residues but only 3 arginine, 1 histidine, and 0 lysine residues. As expected, many of the charged and polar side chains lie on or near the protein surface; therefore, many of these do not possess well-defined conformations. In contrast, many of the hydrophobic residues are buried in the protein interior and display well-ordered conformations. Figure 9 shows a stereoview of superimposed side chains for all Cys, His, Ile, Leu, Met, Phe, Tyr, and Val residues, with the same orientation as that used in Figure 6B.

FIGURE 6: Stereoviews of the superimposed apokedarcidin backbones of the 15 refined NMR structures (black traces). (A, top) A "frontal" view looking into the chromophore binding pocket. The N- and C-termini are labeled. (B, bottom) A "side" view with the chromophore binding pocket facing right. The backbone of the aponeocarzinostatin X-ray structure (Teplyakov et al., 1993) is also shown (heavy red trace).

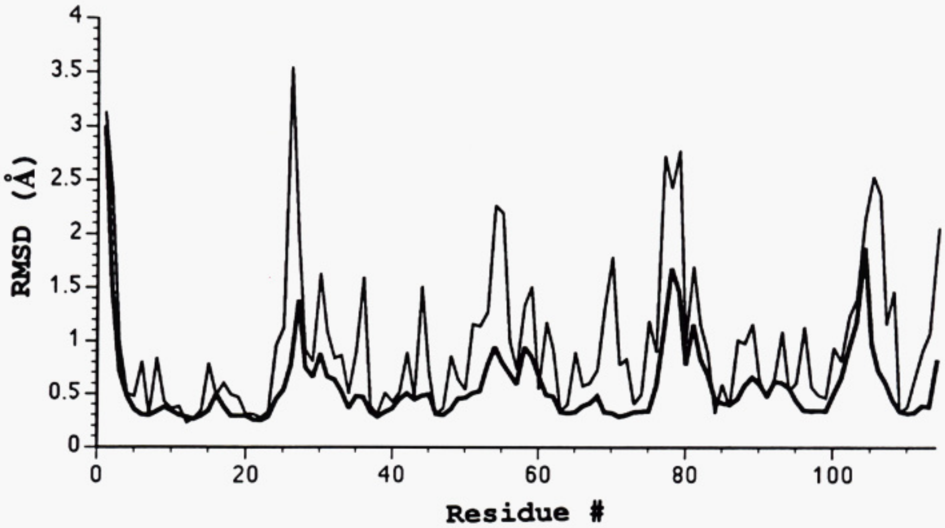

FIGURE 7: Plots of residue-specific RMS displacements for the 15 refined NMR structures. The heavy trace shows the average backbone atom RMSD for each residue between the NMR models and the mean NMR structure after global fitting of backbone atoms. The thinner trace shows the corresponding data for side-chain heavy atoms.

Although most of the hydrophobic residues are well-defined, there are exceptions. For example, Met77 and Tyr106 display high disorder. Both of these residues are solvent exposed in apokedarcidin. Also, they both form part of the edges of the chromophore binding pocket, which we now describe.

The chromophore binding pocket of apokedarcidin is significantly larger than that of aponeocarzinostatin (see Figure 6B). To illustrate this further, several distances

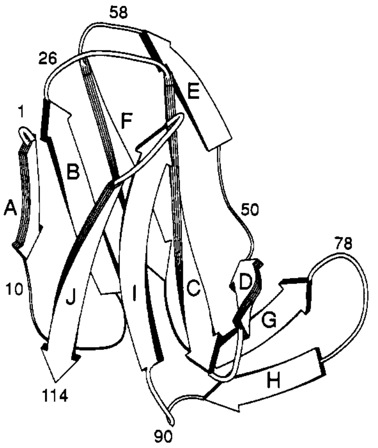

FIGURE 8: Ribbon drawing of the backbone fold of apokedarcidin derived from the best representative NMR structure (see text). The β-strands are indicated by arrows, and selected residue positions are labeled.

between corresponding residues in aponeocarzinostatin and apokedarcidin (Figure 1) are examined. In aponeocarzinostatin the distance between the C^α atom of Gly102 in the upper edge of the binding site and the C^α atom of Gly43 in the β-hairpin at the base of the binding pocket is 13.43 Å. The corresponding distance between the C^α atoms of Gly104 and Gly43 in the mean apokedarcidin NMR structure is 19.32 Å. Likewise, in aponeocarzinostatin the distance between the C^α atoms of Gly102 and Phe78 (in the lower lip of the binding pocket) is 10.32 Å, whereas the corresponding distance between Gly104 and Met77 in the mean apokedarcidin structure is 18.86 Å. These results demonstrate that the kedarcidin chromophore binding site is vertically larger (in the views of Figure 6) than the aponeocarzinostatin chromophore binding pocket. The kedarcidin binding site is also horizontally wider in the view of Figure 6A. For example, in aponeocarzinostatin the distance between the C^α atoms of Phe52 and Ala109 is 15.76 Å, whereas the corresponding distance between Phe52 and Ala110 in the mean apokedarcidin structure is 18.90 Å. Overall, these results are consistent with kedarcidin's considerably larger chromophore. The molecular formulas of the neocarzinostatin and kedarcidin chromophores are $C_{35}H_{33}NO_{12}$ and $C_{53}H_{60}N_3O_{16}Cl$, respectively (Edo et al., 1985; Leet et al., 1993).

A stereoview of a space-filling depiction of the representative apokedarcidin NMR structure is shown in Figure 10. Figure 10 provides a view of the chromphore binding surface. Side chains projecting into the binding pocket or located on its edges include Thr33, Leu35, Cys37, Ile39, Arg44, Cys47, Val49, Phe52, Asp54, Tyr75, Met77, Glu96, Val98, Tyr106, and Asn108. Of the residues contacting the chromophore in the NMR (Tanaka et al., 1993) and/or X-ray (Kim et al., 1993) structures of the neocarzinostatin chromoprotein, only five are conserved in kedarcidin. These are (kedarcidin numbering) Cys37, Cys47, Phe52, Gly80, and Gly104. In neocarzinostatin, key chromophore/protein interactions involving the enediyne ring include sandwiching of the C(2)–C(3) triple bond between the Cys37–Cys47 disulfide and the Phe52 aromatic ring and contact between the C(6)–C(7) triple bond and Phe78. Phe78 may also protect the chromophore C12 from nucleophilic attack (Kim et al., 1993). Since Cys37, Cys47, and Phe52 are conserved in kedarcidin, it is likely that they are involved in similar stabilizing interactions with the kedarcidin chromophore. Neocarzinostatin's Phe78 is replaced by Met77 in kedarcidin (Figure 1). Thus, Met77 may also make hydrophobic contacts with the enediyne ring. As noted above, Met77 is solvent exposed and disordered in apokedarcidin; it may adopt an ordered conformation upon chromophore binding. Other kedarcidin chromophore/protein interactions are more difficult to predict, since both the chromophore and binding site residue composition differ significantly between kedarcidin and neocarzinostatin. Elucidation of these interactions will require determination of the structure of the kedarcidin chromophore/protein complex.

Finally, as noted in the introduction, apokedarcidin has been observed to display proteolytic activity (Zein et al., 1993b). Therefore, an effort has been made to locate potential catalytic sites. The only potential serine protease-like site involves His53, Asp54, and Thr64 or Ser65. However, a repositioning of Asp54 would be required to produce a catalytic triad. There are two other sites that would be consistent with an aspartic protease-like mechanism, which requires spatial proximity of two acidic side chains. One of these involves Asp79 and Glu82, which are part of the β-hairpin (composed of β-strands G and H) that forms the lower lip of the chromphore binding pocket. The other involves Asp87, Asp89, and/or the C-terminal carboxylate of Gly114, which are positioned beneath the chromophore binding site. In future studies, these insights may serve to guide mutagenesis experiments.

CONCLUDING REMARKS

The $^1H^\beta$, $^{13}C^\beta$, and backbone ^1H, ^{13}C, and ^{15}N resonances of apokedarcidin have been assigned by a semiautomated analysis of six multidimensional triple-resonance NMR spectra. The sequential assignments obtained by the semiautomated analysis were confirmed by a "manual" assignment of side-chain resonances. A qualitative analysis of the apokedarcidin secondary structure revealed that apokedarcidin adopts an overall fold similar to that observed for neocarzinostatin, macromomycin, and apoactinoxanthin. A seven-stranded antiparallel β-barrel domain linked to a subdomain composed of two β-hairpin ribbons is observed for all four proteins.

Cross-peaks in the 3D NOESY spectra were assigned in an automated manner, which was assisted by a preliminary model of apokedarcidin based on the aponeocarzinostatin X-ray structure (Teplyakov et al., 1993). This approach is justified by the sequence similarities between kedarcidin and neocarzinostatin (Figure 1) and the very similar secondary structure elements observed for apokedarcidin (Figure 5) and aponeocarzinostatin (Remerowski et al., 1990; Gao & Brukhart, 1991). A total of 785 NOE distance constraints and 112 dihedral angle constraints were used to generate 160 models of the apokedarcidin solution structure using the DIANA program (Güntert et al., 1991; Güntert & Wüthrich, 1991). After structure selection and simulated annealing refinement using the X-PLOR program (Brünger et al., 1992), a set of 15 refined apokedarcidin structures was obtained. This ensemble displays reasonably high resolution. The chromophore binding site of apokedarcidin is larger than that of aponeocarzinostatin; this is probably an adaptation to kedarcidin's larger chromophore (Edo et al., 1985; Leet et al., 1993). The structure of the chromophore binding site of apokedarcidin suggests that interactions similar to those observed in the neocarzinostatin chromoprotein (Tanaka et al., 1993; Kim et al., 1993) may serve to stabilize the enediyne in kedarcidin; however, the remaining protein/chromophore interactions must differ substantially.

A number of NOE cross-peaks remain unassigned in the 3D NOESY spectra of apokedarcidin. Assignment of these

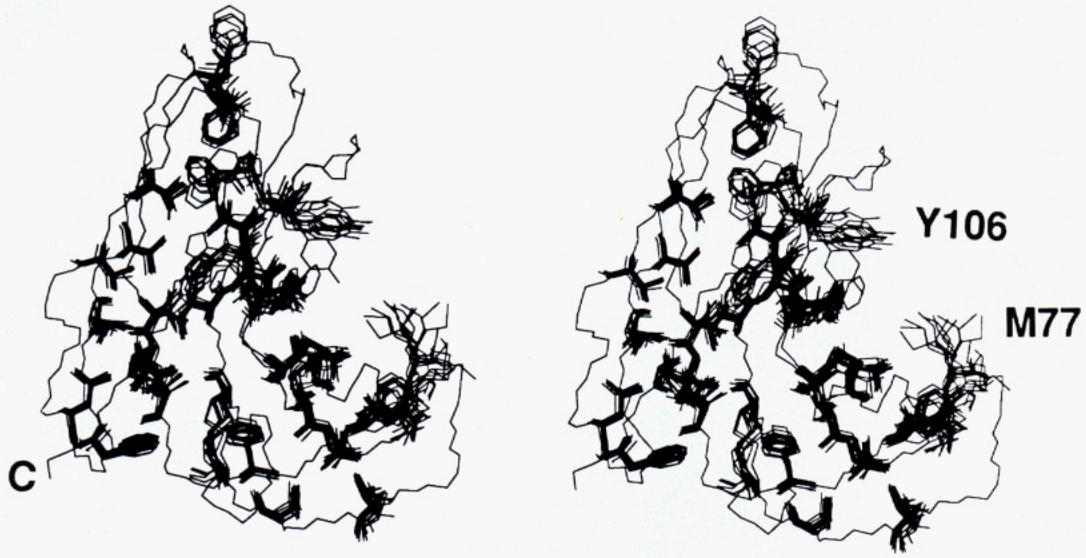

FIGURE 9: Stereoview of the 15 superimposed NMR structures of apokedarcidin showing all Cys, His, Ile, Leu, Met, Phe, Tyr, and Val residues. Met77 and Tyr106 are labeled. The backbone trace of the representative NMR structure (see text) is also shown, with the C-terminus labeled.

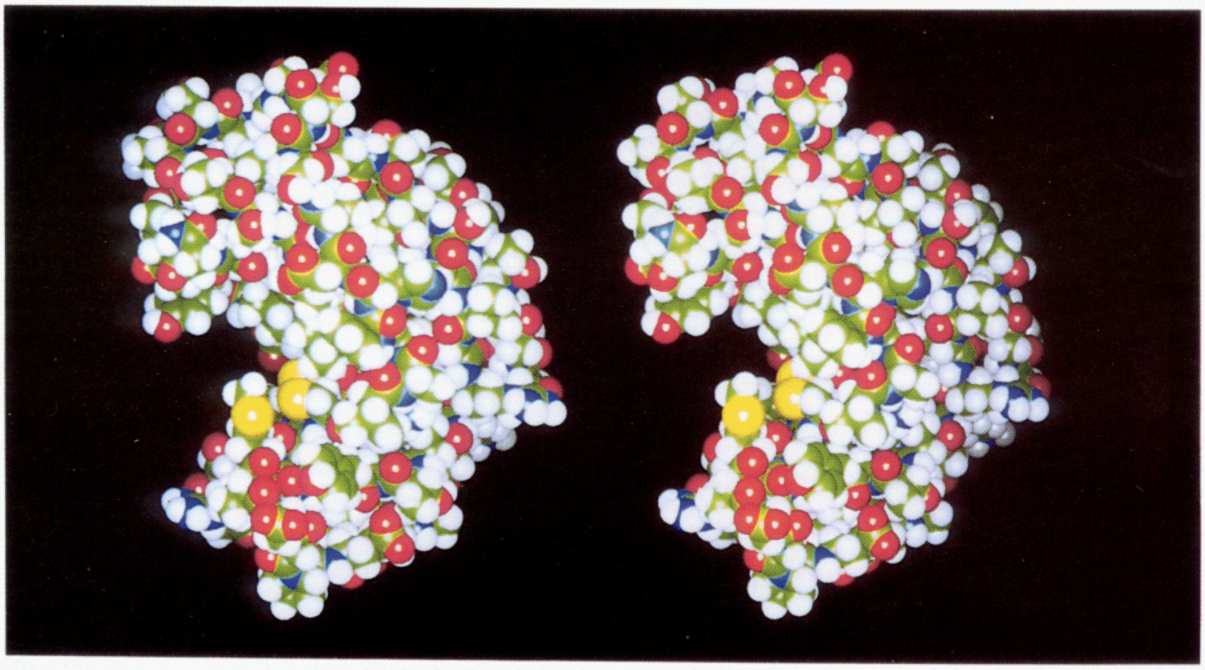

FIGURE 10: Stereoview of the representative NMR model (see text) of apokedarcidin. A space-filling representation of all atoms is displayed, with carbons shown in green, nitrogens shown in blue, oxygens shown in red, sulfurs shown in yellow, and hydrogens shown in white. Met77 and the Cys37–Cys47 disulfide bridge are clearly visible in the chromophore binding site.

cross-peaks may require a time-consuming manual analysis of the 3D NOESY spectra. Also, acquisition and analysis of 4D NOESY spectra (in progress) will provide additional NOE constraints. Only one sealed sample of $^{13}C/^{15}N$-labeled apokedarcidin has been obtained so far, precluding the acquisition of NOESY spectra for a sample in 100% ^2H_2O. Also, ^1H–^2H exchange rates have not been measured, and hydrogen bond distance constraints have not yet been incorporated into the molecular modeling. Recently developed experiments (Grzesiek & Bax, 1993b) allow characterization of amide proton exchange rates without exchanging the protein sample into 100% ^2H_2O. Given these considerations, it should be possible to obtain a high-resolution apokedarcidin solution structure ensemble by incorporating hydrogen bond and additional NOE distance constraints. It will be most informative to compare a high-resolution solution structure of apokedarcidin to a structure of the kedarcidin chromoprotein (work in progress).

ACKNOWLEDGMENT

We thank Richard Dalterio for sample analysis during the purification process and for conducting the chromophore content measurement. We also thank Hans Marquardt and Sandra J. Hofstead for providing primary sequence data for kedarcidin. For information about obtaining the CONGEN program, please contact R. E. Bruccoleri at the above address or by e-mail at bruc@bms.com.

SUPPLEMENTARY MATERIAL AVAILABLE

Table S-1 giving ^1H, ^{13}C, and ^{15}N NMR assignments for apokedarcidin at 20 °C, pH 5.4, Table S-2 giving dihedral angle constraints (X-PLOR input file) used to determine the apokedarcidin solution structure, Table S-3 giving NOE distance constraints (X-PLOR input file using average = sum option) for apokedarcidin, Figure S-1 showing the gradient-enhanced ^{15}N-correlated 3D NOESY pulse sequence, Figure S-2 showing the gradient-enhanced 3D ^{13}C-separated NOESY pulse sequence, Figure S-3 showing the NH_2-filtered CxCy-(CO)NH_2 pulse sequence, Figure S-4 showing the CxCy-(CO)NH_2 spectrum of apokedarcidin, and Figure S-5 showing strip plots of the (H)C(CO)NH-TOCSY spectrum of apokedarcidin (44 pages). Ordering information is given on any current masthead page.

REFERENCES

Adjadj, E., Mispelter, J., Quiniou, E., Dimicoli, J.-L., Favaudon, V., & Lhoste, J.-M. (1990) *Eur. J. Biochem. 190*, 263–271.

Adjadj, E., Quiniou, E., Mispelter, J., Favaudon, V., & Lhoste, J.-M. (1992) *Eur. J. Biochem. 203*, 505–511.

Archer, S. J., Ikura, M., Torchia, D. A., & Bax, A. (1991) *J. Magn. Reson. 95*, 636–641.

Bax, A., Clore, G. M., & Gronenborn, A. M. (1990) *J. Magn. Reson. 88*, 425–431.

Billeter, M., Neri, D., Otting, G., Qian, Y. Q., & Wüthrich, K. (1992) *J. Biomol. NMR 2*, 257–274.

Brooks, B. R., Bruccoleri, R. E., Olafson, B. D., States, D. J., Swaminathan, S., & Karplus, M. (1983) *J. Comput. Chem. 4*, 187–217.

Bruccoleri, R. E. (1990) *CONGEN (Version 2.0) Manual*, Bristol-Myers Squibb Pharmaceutical Research Institute, Princeton, NJ.

Bruccoleri, R. E. (1993) *Mol. Simul. 10*, 151–174.

Bruccoleri, R. E., & Karplus, M. (1987) *Biopolymers 26*, 137–168.

Bruccoleri, R. E., Haber, E., & Novotny, J. (1988) *Nature 335*, 564–568.

Brünger, A. T. (1992) *X-PLOR (Version 3.1) Manual*, Yale University Press, New Haven, CT.

Chimura, H., Ishizuka, M., Hamada, M., Hori, S., Kimura, K., Iwanaga, J., Takeuchi, T., & Umezawa, H. (1968) *J. Antibiot. 21*, 44–49.

Clore, G. M., Bax, A., Driscoll, P. C., Wingfield, P. T., & Gronenborn, A. M. (1990) *Biochemistry 29*, 8172–8184.

Constantine, K. L., Madrid, M., Banyai, L., Trexler, M., Patthy, L., & Llinas, M. (1992) *J. Mol. Biol. 223*, 281–298.

Constantine, K. L., Goldfarb, V., Wittekind, M., Friedrichs, M. S., Anthony, J., Ng, S.-C., & Mueller, L. (1993) *J. Biomol. NMR 3*, 41–54.

Constantine, K. L., Friedrichs, M. S., & Mueller, L. (1994a) *J. Magn. Reson. B104*, 62–68.

Constantine, K. L., Friedrichs, M. S., Metzler, W. M., Wittekind, M., Hensley, P., & Mueller, L. (1994b) *J. Mol. Biol. 236*, 310–327.

Edo, K., Mizugaki, M., Koide, Y., Seto, H., Furihata, K., Otake, N., & Ishida, N. (1985) *Tetrahedron Lett. 26*, 331–334.

Fairbrother, W. J., Palmer, A. G., Rance, M., Reizer, J., Saier, M. H., & Wright, P. E. (1992) *Biochemistry 31*, 4413–4425.

Friedrichs, M. S., Mueller, L., & Wittekind, M. (1994) *J. Biomol. NMR* (in press).

Gao, X (1992) *J. Mol. Biol. 225*, 125–135.

Gao, X., & Burkhart, W. (1991) *Biochemistry 30*, 7730–7739.

Gibson, B. W., Herlihy, W. C., Samy, T. S. A., Hahm, K. S., Maeda, H., Meienhofer, J., & Biemann, K. (1984) *J. Biol. Chem. 259*, 10801–10806.

Goldberg, I. H. (1991) *Acc. Chem. Res. 24*, 191–198.

Golik, J., Clardy, J., Dubay, G., Groenewold, G., Kawaguchi, H., Konishi, M., Krishnan, B., Ohkuma, H., Saitoh, K., & Doyle, T. W. (1987a) *J. Am. Chem. Soc. 109*, 3461–3462.

Golik, J., Clardy, J., Dubay, G., Groenewold, G., Kawaguchi, H., Konishi, M., Krishnan, B., Ohkuma, H., Saitoh, K., & Doyle, T. W. (1987b) *J. Am. Chem. Soc. 109*, 3462–3464.

Grzesiek, S., & Bax, A. (1993a) *J. Biomol. NMR 3*, 185–204.

Grzesiek, S., & Bax, A. (1993b) *J. Biomol. NMR 3*, 627–638.

Grzesiek, S., Anglister, J., & Bax, A. (1993) *J. Magn. Reson. B101*, 114–119.

Güntert, P., & Wüthrich, K. (1991) *J. Biomol. NMR 1*, 447–456.

Güntert, P., & Wüthrich, K. (1991) *J. Biomol. NMR 1*, 447–456.

Güntert, P., Braun, W., & Wüthrich, K. (1991) *J. Mol. Biol. 217*, 517–530.

Hanada, M., Ohkuma, H., Yonemoto, T., Tomita, K., Ohbayashi, M., Kamei, H., Miyaki, T., Konishi, M., Kawaguchi, H., & Forenza, S. (1991) *J. Antibiot. 44*, 403–414.

Hansen, P. E. (1991) *Biochemistry 30*, 10457–10466.

Hensens, O. D., & Goldberg, I. H. (1989) *J. Antibiot. 42*, 761–768.

Hensens, O. D., Giner, J. L., & Goldberg, I. H. (1989) *J. Am. Chem. Soc. 111*, 3295–3299.

Hidaka, T., Yano, Y., Yamashita, T., & Watanabe, K. (1979) *J. Antibiot. 32*, 340–346.

Hofstead, S. J., Matson, J. A., Malacko, A. R., & Marquardt, H. (1992) *J. Antibiot. 45*, 1250–1254.

Kay, L. E., Ikura, M., & Bax, A. (1990) *J. Am. Chem. Soc. 112*, 888–889.

Kay, L. E., Wittekind, M., McCoy, M. A., Friedrichs, M. S., & Mueller, L. (1992) *J. Magn. Reson. 98*, 443–450.

Kay, L. E., Xu, G.-Y., Singer, A. U., Muhandiran, D. R., & Forman-Kay, J. D. (1993) *J. Magn. Reson. B101*, 333–337.

Khokhlov, A. S., Cherches, B., Reshetov, P. D., Smirnova, G. M., Sorokina, I. B., Prokoptzeva, T. A., Koloditskaya, T. A., Smirnov, V. V., Navashin, S. M., & Formina, I. P. (1969) *J. Antibiot. 22*, 541–544.

Khokhlov, A. S., Reshetov, P. D., Chupova, L. A., Cherches, B. Z., Zhigis, L. S., & Stoyachenko, I. A. (1976) *J. Antibiot. 29*, 1026–1034.

Kim, K.-H., Kwon, B.-M., Myers, A. G., & Rees, D. C. (1993) *Science 262*, 1042–1046.

Kline, T. P., Brown, F. K., Brown, S. C., Jeffs, P. W., Kopple, K. D., & Mueller, L. (1990) *Biochemistry 29*, 7805–7813.

Konishi, M., Ohkuma, H., Matsumoto, K., Kamei, H., Miyaki, T., Tsuno, T., Oki, T., Kawaguchi, H., VanDuyne, G. D., & Clardy, J. (1989) *J. Antibiot. 42*, 1449–1452.

Kumada, Y., Miwa, T., Naoi, N., Watanabe, K., Naganawa, H., Takita, T., Umezawa, H., Nakamura, H., & Iitaka, Y. (1983) *J. Antibiot. 36*, 200–202.

Lam, K. S., Hesler, G. A., Gustavson, D. R., Crosswell, A. R., Veitch, J. M., & Forenza, S. (1991) *J. Antibiot. 44*, 472–478.

Laskowski, R. A., MacAuthor, M. W., Moss, D. S., & Thornton, J. M. (1993) *J. Appl. Crystallogr. 26*, 283–291.

Lee, M. C., Dunne, T. S., Chang, C. C., Siegel, M. M., Ellestad, G. A., Morton, G. O., McGahren, W. J., & Borders, D. B. (1992) *J. Am. Chem. Soc. 114*, 985–997.

Leet, J. E., Schroeder, D. R., Hofstead, S. J., Golik, J., Colson, K. L., Huang, S., Klohr, S. E., Doyle, T. W., & Matson, J. A. (1992) *J. Am. Chem. Soc. 114*, 7946–7948.

Leet, J. E., Schroeder, D. R., Langley, D. R., Colson, K. L., Huang, S., Klohr, S. E., Lee, M. S., Golik, J., Hofstead, S. J., Doyle, T. W., & Matson, J. A. (1993) *J. Am. Chem. Soc. 115*, 8432–8443.

Logan, T. M., Olejniczak, E. T., Xu, R. X., & Fesik, S. W. (1992) *FEBS Lett. 314*, 413–418.

McCoy, M. A., & Mueller, L. (1992a) *J. Am. Chem. Soc. 114*, 2108–2112.

McCoy, M. A., & Mueller, L. (1992b) *J. Magn. Reson. 98*, 674–679.

Metzler, W. J., Constantine, K. L., Friedrichs, M. S., Bell, A. J., Ernst, E. G., Lavoie, T. B., & Mueller, L. (1993) *Biochemistry 32*, 13818–13829.

Montelione, G. T., Lyons, B. A., Emerson, S. D., & Tashiro, M. (1992) *J. Am. Chem. Soc. 114*, 10974–10975.

Nicolaou, K. C., & Dai, W. M. (1991) *Angew. Chem., Int. Ed. Engl. 30*, 1387–1416.

Nilges, M., Gronenborn, A. M., Brünger, A. T., & Clore, G. M. (1988) *Protein Eng. 2*, 27–38.

Olejniczak, E. T., Xu, R. X., Petros, A. M., & Fesik, S. W. (1992) *J. Magn. Reson. 100*, 444–450.

Otani, T. (1993) *J. Antibiot. 46*, 791–802.

Pletnev, V. Z., Kuzin, A. P., Trakhanov, S. D., & Kostetsky, P. V. (1982) *Biopolymers 21*, 287–300.

Remerowski, M. L., Glaser, S. J., Sieker, L. C., Samy, T. S. A., & Drobny, G. P. (1990) *Biochemistry 29*, 8401–8409.

Richardson, J. S., & Richardson, D. C. (1989) in *Prediction of Protein Structure and the Principles of Protein Conformation* (Fasman, G. D., Ed.) pp 1–98, Plenum Press, New York.

Sakata, N., Ikeno, S., Hori, M., Hamada, M., & Otani, T. (1992) *Biosci., Biotechnol., Biochem. 10*, 1592–1595.

Samy, T. S. A., Hahm, K.-S., Modest, E. J., Lampman, G. W., Keutmann, H. T., Umezawa, H., Herlihy, W. C., Gibson, B. W., Carr, S. A., & Biemann, K. (1983) *J. Biol. Chem. 258*, 183–191.

Schwabe, J. W. R., Chapman, L., Finch, J. T., Rhodes, D., & Neuhaus, D. (1993) *Structure 1*, 187–204.

Shaka, A. J., Lee, C. J., & Pines, A. (1988) *J. Magn. Reson. 77*, 274–293.

Spera, S., & Bax, A. (1991) *J. Am. Chem. Soc. 113*, 5490–5492.

Tanaka, T., Hirama, M., Fujita, K., Imajo, S., & Ishiguro, M. (1993) *Chem. Commun. 15*, 1205–1207.

Teplyakov, A., Obmolova, G., Wilson, K., & Kuromizu, K. (1993) *Eur. J. Biochem. 213*, 737–741.

Van Roey, P., & Beerman, T. A. (1989) *Proc. Natl. Acad. Sci. U.S.A. 86*, 6587–6591.

Wishart, D. S., Sykes, B. D., & Richards, F. M. (1991) *J. Mol. Biol. 222*, 311–333.

Wittekind, M., & Mueller, L. (1993) *J. Magn. Reson. B101*, 201–205.

Wittekind, M., Gorlach, M., Friedrichs, M. S., Dreyfuss, G., & Mueller, L. (1992) *Biochemistry 31*, 6254–6265.

Wittekind, M., Metzler, W. J., & Mueller, L. (1993) *J. Magn. Reson. B101*, 214–217.

Wüthrich, K. (1986) *NMR of Proteins and Nucleic Acids*, John Wiley & Sons, New York.

Wüthrich, K., Billeter, M., & Braun, W. (1983) *J. Mol. Biol. 169*, 949–961.

Yamashita, T., Naoi, N., Hikada, T., Watanabe, K., Kumada, Y., Takeuchi, T., & Umezawa, H. (1979) *J. Antibiot. 32*, 330–339.

Yamazaki, T., Forman-Kay, J. D., & Kay, L. E. (1993) *J. Am. Chem. Soc. 115*, 11054–11055.

Zaheer, A., Zaheer, S., & Montegomery, R. (1985) *J. Biol. Chem. 260*, 11787–11792.

Zein, N., Colson, K. L., Leet, J. E., Schroeder, D. R., Solomon, W., Doyle, T. W., & Casazza, A. M. (1993a) *Proc. Natl. Acad. Sci. U.S.A. 90*, 2822–2826.

Zein, N., Casazza, A. M., Doyle, T. W., Leet, J. E., Schroeder, D. R., Solomon, W., & Nadler, S. G. (1993b) *Proc. Natl. Acad. Sci. U.S.A. 90*, 8009–8012.

Zhu, G., & Bax, A. (1990) *J. Magn. Reson. 90*, 405–410.